Journal of Materials Chemistry A

ROYAL SOCIETY OF CHEMISTRY

PAPER

View Article Online
View Journal

Cite this: DOI: 10.1039/d5ta05321h

Accelerating the discovery of disordered multi-component solid-state electrolytes using machine learning interatomic potentials

Yanhao Deng, [a] Yan Li,[a] Gopalakrishnan Sai Gautam, [b] Bonan Zhu *[cd] and Zeyu Deng *[a]

Received 1st July 2025
Accepted 4th September 2025

DOI: 10.1039/d5ta05321h

rsc.li/materials-a

Machine learning interatomic potentials (MLIPs) are rapidly emerging as powerful tools for materials simulations, offering a promising pathway to explore complex systems beyond the reach of traditional methods. This study investigates the application of MLIPs focused on the MACE architecture, to multi-component, disordered solid-state electrolytes (SSEs), a critical class of materials for the next-generation solid-state batteries. We first benchmark the performance of MACE against established SSE families, $Na_{1+x}Zr_2Si_xP_{3-x}O_{12}$ and $Li_{3+x}P_{1-x}Ge_xS_{4-4x}O_{4x}$, confirming their general applicability while identifying key considerations for robust potential development in chemically diverse systems. This workflow, emphasizing the selection of representative configurations, provides critical insights for constructing reliable models in complex, multi-components environments. We further demonstrate the predictive power of this approach by constructing a high-performance MLIP for the novel halide system $Li_3In_xY_{1-x}Br_{6y}Cl_{6-6y}$ ($x, y \in [0, 1]$ and $x + y \geq 1$), leading to the identification of the $Li_3In_{0.5}Y_{0.5}Br_3Cl_3$ stoichiometry with the most favorable predicted ion transport properties. By analyzing the molecular dynamics (MD) trajectories generated in this work using our MLIP, we identified two distinct Li-ion migration pathways in this material. The trained model facilitates the computational investigation of intricate mixed cation/anion substitutions in halide SSEs, offering new insights into higher-entropy systems incorporating multi-components. Our results underscore the capability of MLIPs to accelerate the discovery cycle of complex functional materials and provide a robust computational framework for designing advanced SSEs.

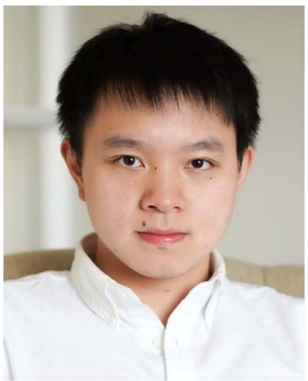

Zeyu Deng

Dr Zeyu Deng (also known as Jerry) is an Assistant Professor in the Department of Materials Science and Engineering at the National University of Singapore (NUS). He received his MPhil and PhD in Materials Science and Metallurgy from the University of Cambridge, followed by post-doctoral research at NUS. Dr Deng specialises in computational materials science, multi-scale modelling, and high-performance computing, focusing on materials for renewable energy, energy storage, and CO_2 capture. His achievements include the Lee Kuan Yew Post-doctoral Fellowship (2022) and the MRS Graduate Student Award (2018).

Introduction

Combining quantum precision with classical efficiency, machine learning interatomic potentials (MLIPs) are emerging as transformative tools in computational materials science[1,2] that enable simulations several orders of magnitude faster than *ab initio* methods.[3,4] This dual advantage of enhanced speed and reliable accuracy enables the computational investigation of complex material systems and large-length, long-time scale molecular dynamics (MD) simulations, significantly broadening the horizons of computational materials research.[5,6]

MLIPs have been developed based on approaches such as the Gaussian approximation potential (GAP),[7] moment tensor potentials (MTP),[8] and neural network models.[9,10] Graph Neural Networks (GNNs)[11] have become a widely used framework for modeling atomic systems and developing interatomic potentials. Notable examples include CGCNN,[12] M3GNet,[13] and CHGNet.[14] By encoding structural symmetry information, invariant and particularly equivariant GNNs—such as NequIP[15]

[a]Department of Materials Science and Engineering, National University of Singapore, 9 Engineering Drive 1, 117575, Singapore. E-mail: msedz@nus.edu.sg
[b]Department of Materials Engineering, Indian Institute of Science, Bengaluru 560012, India
[c]School of Aerospace Engineering, Beijing Institute of Technology, Beijing, 100081, China. E-mail: bzhu@bit.edu.cn
[d]State Key Laboratory of Environment Characteristics and Effects for Near-space, Beijing, 100081, China

and MACE[16]—have achieved enhanced efficiency without compromising accuracy.[17,18] The MACE architecture,[16] which extends the atomic cluster expansion (ACE) framework[19] and employs high body-order equivariant features in each layer, enabling accurate modeling with just two layers of message passing, thus achieving low computational cost, on the order of nanoseconds per day on a GPU.

Meanwhile, training universal MLIPs (uMLIPs) using large, diverse datasets such as the Materials Project (MP),[20] AFLOW,[21] Open Quantum Materials Database (OQMD),[22] Alexandria,[23] Open Materials 2024 (OMAT24),[24] and MatPES[25] has generated significant interest, enabling direct deployment across materials encompassing >90% of application-relevant elements in the periodic table, including inorganic crystals, organic compounds, and theoretically predicted structures.[5,13] As their reliability and generalizability improve, uMLIPs are rapidly becoming mainstream tools for materials modeling.[26–28] Recent state-of-the-art uMLIPs, such as MACE-MP,[29] eSEN,[30] SevenNet,[17] and BAMBOO,[31] training on those diverse and combined datasets, enable transferability across a wide range of materials systems.

In this work, we systematically evaluate the performance of the MACE architecture by fine-tuning the MACE-MP (version: MACE-MP-0a).[29] We apply this model to representative SSEs, which are crucial for advancing safer lithium- and sodium-based batteries by replacing conventional flammable liquid electrolytes with solid fast-ion conductors.[32–34] While there have been increasing applications of MLIPs in modeling SSEs,[4,35–41] achieving broad compositional coverage, low computational cost, high prediction accuracy, and fidelity remains challenging.[42] To address this, fine-tuning a uMLIP offers a promising strategy, as it enables adaptation to new material systems with minimal additional data while leveraging knowledge from diverse chemistries. We implement this scheme by fine-tuning the MACE-MP model using a multi-head strategy, which requires only a small dataset to achieve stable results and helps prevent catastrophic forgetting that can occur during naive fine-tuning. Furthermore, an efficient training data selection algorithm is introduced to further enhance the effectiveness of this fine-tuning process.

As a benchmark system, we first evaluate the model on $Na_{1+x}Zr_2Si_xP_{3-x}O_{12}$ (NaSICON), a class of SSEs first reported more than 40 years ago.[43] Its extensive experimental and computational history makes it an ideal candidate to validate the MLIP performance and reconcile predictions with previous studies.[43–49] Our investigation also includes materials from the oxysulfide SSE family. Specifically, we focus on the pseudo-binary system $(1-x)Li_3PS_4$–xLi_4GeO_4 (LPSGO).[50] This system aims to combine the high Li-ion conductivity of sulfides like Li_3PS_4 (LPS) with the electrochemical stability of oxides like Li_4GeO_4 (LGO), offering an excellent platform to assess the ability of MLIPs to capture complex hybrid SE chemistries.

Beyond these benchmarks, our investigation extends to lithium ternary halide systems (Li_3MX_6), with a focus on the mixed halide system represented by the ternary compound phase diagram Li_3YBr_6–Li_3InBr_6–Li_3InCl_6. Each compound serves as a vertex of a compositional triangle. This ternary system is described by the general chemical formula $Li_3In_xY_{1-x}Br_{6y}Cl_{6-6y}$, where $x, y \in [0, 1]$ and $x + y \geq 1$. Among these, Li_3InBr_6 exhibits high room-temperature conductivity (0.1–1 mS cm^{-1}),[51–53] while Li_3YBr_6 achieves similar performance (0.03–1.7 mS cm^{-1}).[54] Recently, Li_3InCl_6 has demonstrated excellent ionic conductivity (0.79–4.03 mS cm^{-1}) and excellent chemical and electrochemical stability, benefiting from reduced grain boundary effects.[55–59] Although simple mixed-halide SSEs (*e.g.*, $Li_3InBr_xCl_{6-x}$) are well-studied, investigating complex cases involving simultaneous double elemental substitutions (where $x \neq 0$ and $y \neq 0$ in $Li_3In_xY_{1-x}Br_{6y}Cl_{6-6y}$) remains challenging. Herein, leveraging MACE architecture, we demonstrate that a single, fine-tuned model can accurately capture the entire energy landscape across this quaternary compositional space, including experimentally unexplored regions, thereby facilitating the discovery of new high-performance compositions.

Results

It is widely recognized that the distribution of the training dataset significantly influences the performance of MLIP models.[60] To construct a comprehensive training dataset for a disordered, multi-component system, we developed a robust workflow, as illustrated in the upper panel of Fig. 1. First, we enumerate possible structures for each distinct composition within the investigated chemical system. Their energies were estimated using the uMLIP (MACE-MP), enabling the construction of a thermodynamic convex hull across the entire compositional space. Structures were then selected probabilistically based on their energy above the convex hull (E_{hull}) per formula unit, with a probability proportional to the Boltzmann factor, $p \propto \exp(-E_{\text{hull}}/k_BT)$, where k_B is the Boltzmann constant. In this study, the temperature T for the Boltzmann distribution was set to 800 K. This probabilistic approach ensures a realistic balance between highly stable, low-energy configurations and

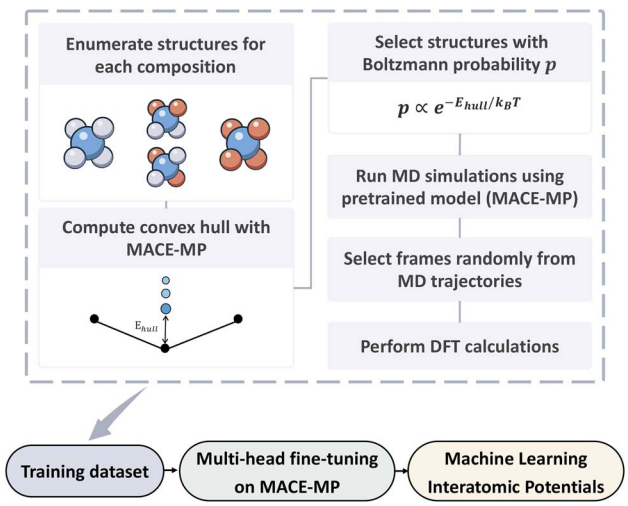

Fig. 1 Workflow for fine-tuning the MLIPs developed in this work. The upper panel (in a dashed box) illustrates the procedure for constructing the training dataset.

thermodynamically accessible higher-energy structures, reflecting their thermal population. Additionally, the lowest-energy structure for each composition was always included to guarantee complete baseline coverage in the dataset.

Subsequently, for each selected configuration, we performed MD simulations to sample the potential energy surface under non-equilibrium conditions using the same MACE-MP model in a canonical *NVT* ensemble at 800 K for 15 ps with a 1 fs timestep. The first 5 ps were allocated for equilibration and the remaining 10 ps were used for the production phase. This step aims to comprehensively explore the configuration space of each system. For each MD simulation, 30 structures were randomly selected, resulting in a total of around 2500 structures. A random strain, within ±3%, is also applied for each configuration to enrich the stress values sampled. Finally, single-point DFT calculations were performed on these diverse configurations to construct an accurate training dataset. The strongly constrained and appropriately normed semilocal density functional (SCAN)[61] is employed in these DFT calculations to achieve high fidelity, compared to the Perdew–Burke–Ernzerhof (PBE) functional[62] used in the original MACE-MP model. This multi-fidelity training strategy has been shown to be feasible and effective for improving model accuracy.[6,63] Further methodological details of DFT are provided in the Methodology section.

Benchmark on NaSICON and LPGSO

The first system investigated is NaSICON ($Na_{1+x}Zr_2Si_xP_{3-x}O_{12}$, $x \in [0, 3]$, $\Delta x = 0.25$), focusing on its high-temperature phase in $R\bar{3}c$ (no. 167) space group.[44] The crystal structure of NaSICON is presented in Fig. 2(a). Na ions occupy two partially occupied crystallographic sites – Na(1) and Na(2) – represented as yellow and orange balls, respectively, which contribute to the high ionic conductivity of NaSICON materials.[44] ZrO_6 units are depicted as green polyhedra, while PO_4/SiO_4 polyanionic units are represented as purple polyhedra.

We systematically fine-tune the MACE-MP model with varying training data sizes. Fig. 2(b) illustrates the performance of the model, quantified by the root mean square error (RMSE) on energies, forces, and stresses on the validation set, as a function of training dataset size. As the training dataset size

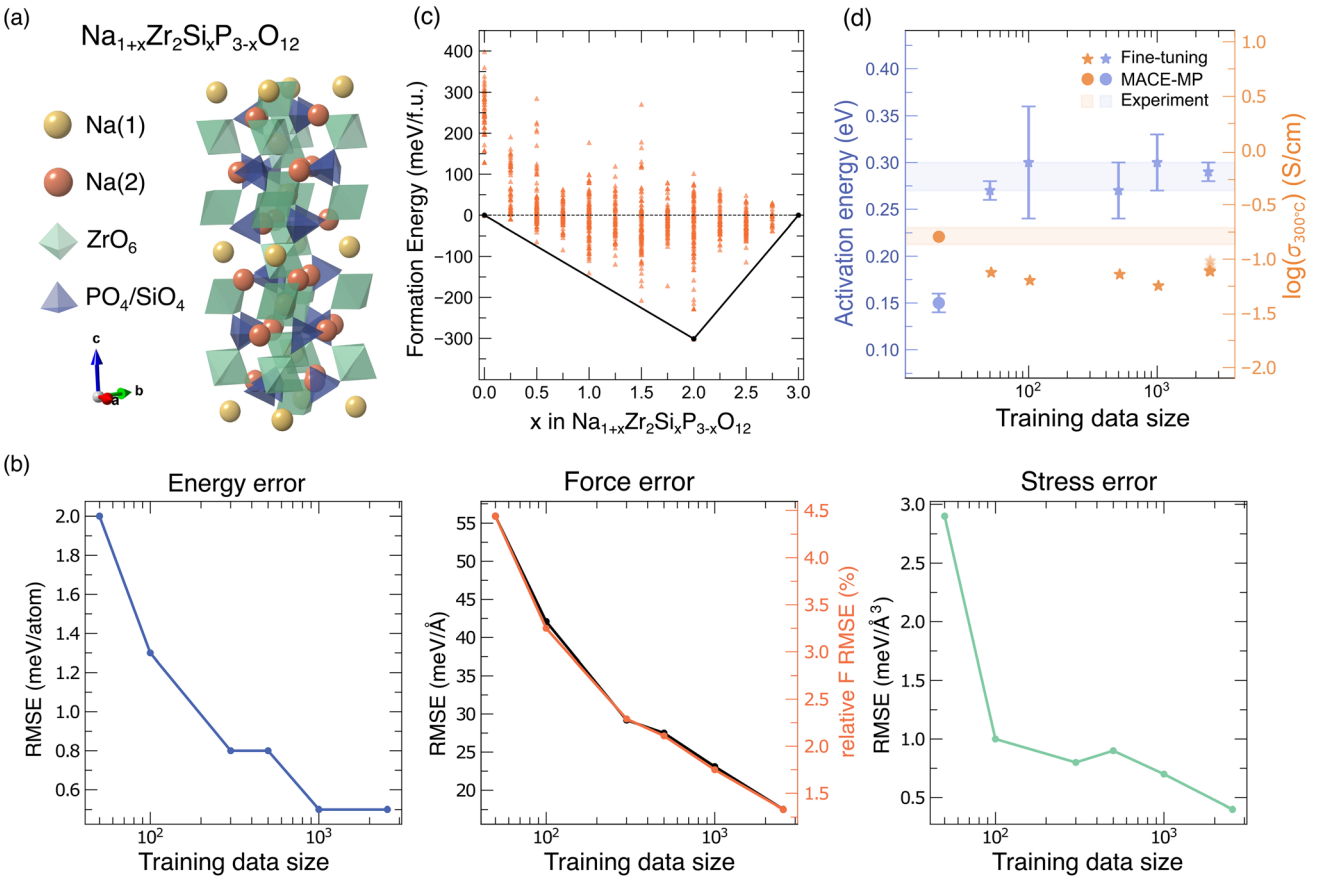

Fig. 2 (a) Crystal structure of $Na_{1+x}Zr_2Si_xP_{3-x}O_{12}$ where Na(1) and Na(2) sites depicted as yellow and orange spheres, respectively. ZrO_6 and PO_4/SiO_4 units are represented as green and purple polyhedra. (b) Quantitative comparison of validation performance between models fine-tuned with different sizes of training dataset. (c) Formation energy (E_f) as a function of composition x in $Na_{1+x}Zr_2Si_xP_{3-x}O_{12}$. The thermodynamic convex hull is shown as black lines, with energies calculated using a model fine-tuned with approximately 2500 DFT calculations. (d) Activation energy barrier and conductivity at 300 °C for $Na_3Zr_2Si_2PO_{12}$ predicted by models trained on datasets of different sizes. Experimental results[43,44] and simulation using MACE-MP without fine-tuning are included. Error bars for activation energy reflect standard deviations from Arrhenius plots (see Methodology section for more details). When the training data size is approximately 2500, structures with different PO_4/SiO_4 orderings are used for MD simulations. The lowest point is calculated from the ground state structure.

increases, the RMSEs of all three properties decrease consistently. In particular, the continued reduction in the RMSEs of force and stress for training dataset sizes above 1000 suggests that additional data augmentation could further enhance the model's accuracy. Given the sufficiently low errors for reliable property predictions (0.5 meV per atom, 17.5 meV $Å^{-1}$, and 0.4 meV $Å^{-3}$ for energy, force, and stress, respectively), we adopt the model fine-tuned with the full dataset of approximately 2500 structures for subsequent calculations. The original MACE-MP model is excluded from this comparison because it is trained with calculated data that uses PBE functional, while we generated the training data for fine-tuning employing SCAN, making direct energy comparisons invalid.

The formation energy and phase stability of $Na_{1+x}Zr_2Si_xP_{3-x}O_{12}$ are predicted, as shown in Fig. 2(c). Three stable compositions at $x = 0$, 2, and 3 are identified, consistent with the previous work.[44] We then evaluate the performance of fine-tuned models as a function of training dataset size and compare it with the MACE-MP model. Specifically, we examine the ionic conductivity of the ground-state structure of $Na_3Zr_2Si_2PO_{12}$, comparing our findings with experimental results[43,44] (Fig. 2(d) and Table S1). The Arrhenius plots obtained by MACE-MP and each fine-tuned model are shown in Fig. S1. The results indicate that the activation energies predicted by the various fine-tuned models, even with limited training data, align well with experimental measurements to within a difference of 0.02 eV. Furthermore, the calculated ionic conductivities at 300 °C also show approximate order-of-magnitude consistency with experimental observations.

Moreover, Fig. 2(d) suggests that increasing the training data size of the fine-tuned model generally leads to more stable predictions and smaller errors in the estimated activation energy. While the original MACE-MP model predicts $\sigma_{300°C}$ with the highest accuracy among all models, its activation energy deviates significantly from the experimental values, about 0.15 eV lower. The conductivities predicted by the fine-tuned models are stable across different training data sizes. The difference between the predicted and experimental conductivity values is small and acceptable, at 0.05–0.12 S cm^{-1}. While there are some differences—potentially due to variations in the exchange–correlation functionals used to calculate the training data—the results are still reasonable, especially considering that the activation energy predictions demonstrate even greater precision. We also analyzed the MD trajectory of Na ions in $Na_3Zr_2Si_2PO_{12}$ at 800 K using GEMDAT software.[64] The shape of the probability density (Fig. S2) is consistent with the literature.[65] Besides, it has been reported that different PO_4/SiO_4 orderings can lead to variations in ionic conductivity (Fig. S3).[44] To provide further validation, a series of $Na_3Zr_2Si_2PO_{12}$ configurations were generated using a Monte Carlo (MC) sampling approach[37] on a $4 \times 4 \times 4$ supercell. Subsequent MD simulations were performed on these structures, using the potential model trained on a dataset of 2500 points. The resulting ionic conductivities, presented in Fig. 2(d) (in transparent orange star points), demonstrate a clear increase from 0.08 S cm^{-1} to about 0.1 S cm^{-1} for the MC phases relative to the crystalline ground state.

Overall, using the NaSICON system as a benchmark, we demonstrate that fine-tuning with an appropriately sized dataset enables predictions comparable to experimental results. Our findings suggest that datasets of approximately 2500 structures provide a reliable balance between computational feasibility and predictive precision for NaSICON material, while a careful convergence test is always needed.

For the LPGSO system, we adopted structures for $Li_{3+x}P_{1-x}Ge_xS_{4-4x}O_{4x}$ ($x \in [0, 1]$) from the work of Li *et al.*, where *Pnma* (no. 62) phase is used as the host model for both parent materials β-Li_3PS_4 and Li_4GeO_4 (Fig. 3(a)).[50] The same strategy has been adopted for creating the training dataset from $x \in [0, 1]$, $\Delta x = 0.125$, comprising approximately 2500 structures in total. A convergence test was also performed to determine the optimal training data size for the fine-tuned model (Fig. S4).

The formation energies of $Li_{3+x}P_{1-x}Ge_xS_{4-4x}O_{4x}$ compositions as predicted by the trained MLIP, are presented in Fig. 3(b). These results exhibit a convex hull profile closely resembling the DFT-calculated results obtained using the SCAN functional.[50] Most importantly, our model predicts a stable phase $Li_{3.5}P_{0.5}Ge_{0.5}S_2O_2$, which possesses the same structure and ordering as the DFT calculations and exhibits similar formation energy (−178 meV per atom for the fine-tuned model compared to −182 meV per atom from DFT). Furthermore, for its Li-ion kinetics, the model yields an activation energy of ∼0.29 eV for $Li_{3.5}P_{0.5}Ge_{0.5}S_2O_2$, as shown in Fig. 3(d). Since this material remains unexplored experimentally, we compare the predicted ionic conductivities with those obtained from previous *ab initio* molecular dynamics (AIMD) simulations.[50,68] These AIMD results exhibit discrepancies with conductivities spanning orders of magnitude, whereas our model predicts values that lie between these extremes while showing good agreement in activation energies.

Given the computational efficiency of fine-tuned models, which offers a distinct advantage over traditional, more expensive DFT simulations, it is of significant interest to examine all available phases of Li_3PS_4 beyond the β polymorph specifically investigated in the LPGSO system, to test the generalizability. It is known that Li_3PS_4 exhibits three distinct phases at different temperatures: the room-temperature γ phase ($Pmn2_1$), which transitions to the β phase (*Pnma*) at 573 K, and subsequently to the α phase (*Cmcm*) at 746 K.[66,67,70–73] Here, the ionic conductivity of the two high-temperature phases of Li_3PS_4 (α and β) is plotted in Fig. 3(c). The predicted ionic conductivities align closely with experimental measurements, as evidenced by the near-overlap of theoretical and experimental data. Specifically, the predicted activation energies are ∼0.26 eV for the α phase and ∼0.44 eV for the β phase. These values compare favorably to experimental values of 0.20 eV and 0.41 eV for the α and β phases, respectively. Fig. S5 illustrates the probability density isosurface of Li ion diffusion in β-Li_3PS_4. The data, which was extracted from MLIP-MD simulations performed with our fine-tuned model, demonstrates migration pathways in good agreement with previous analysis by Kim *et al.*[74]

While the *Pnma* phase is consistently used as the host structural model in the LPGSO system, it is important to note

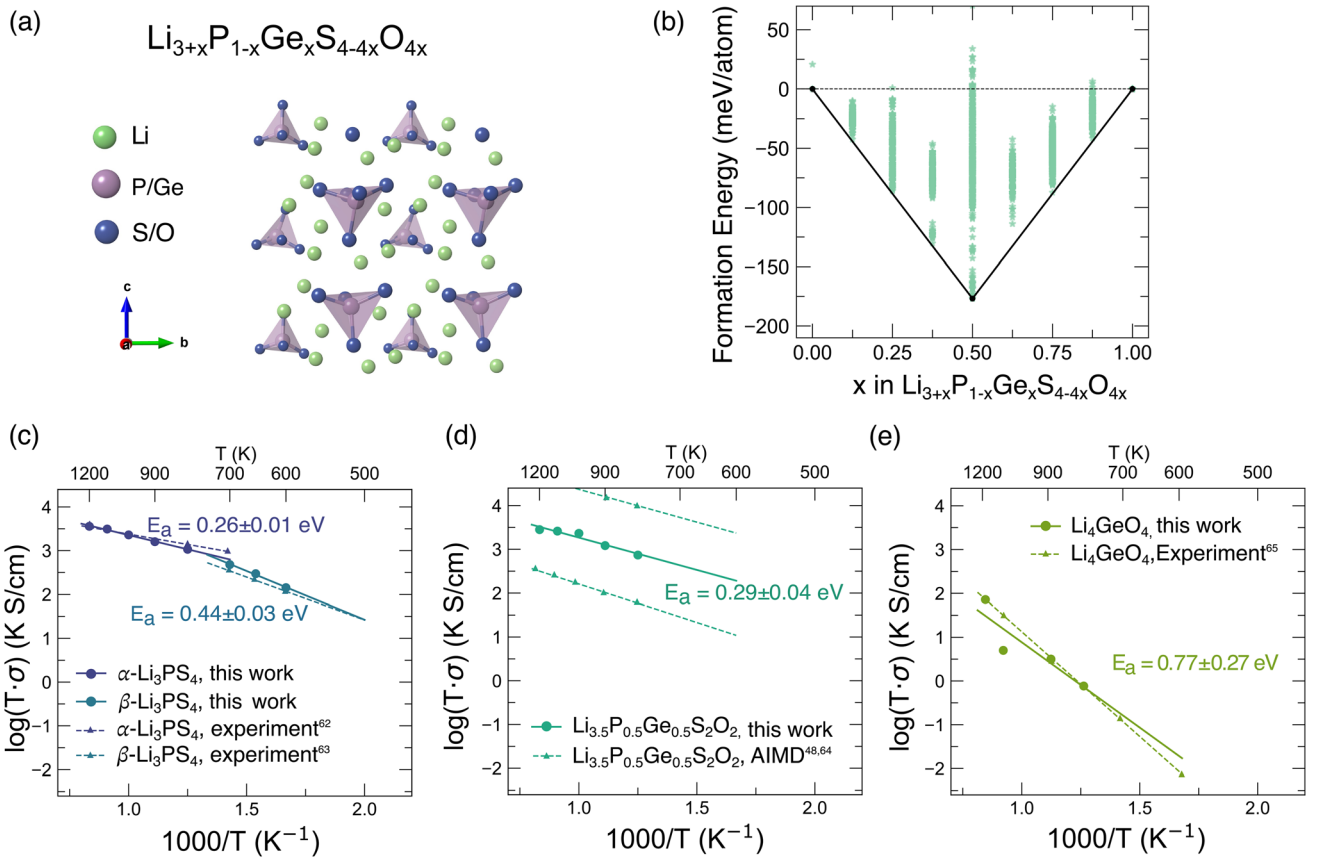

Fig. 3 (a) Crystal structure of $Li_{3+x}P_{1-x}Ge_xS_{4-4x}O_{4x}$ in the *Pnma* space group. Li atoms are depicted by green spheres, P/Ge atoms as purple, and S/O atoms as dark blue. (b) Computed formation energy, E_f, as a function of composition x in $Li_{3+x}P_{1-x}Ge_xS_{4-4x}O_{4x}$. Thermodynamically stable structures are marked by black points on the convex hull. (c–e) Comparison of activation energies (E_a) and ionic conductivities (σ) between our model and reference (AIMD and/or experiments) values for (c) Li_3PS_4,[66,67] (d) $Li_{3.5}P_{0.5}Ge_{0.5}S_2O_2$,[50,68] and (e) Li_4GeO_4 (*Cmcm*).[69] Experimental and AIMD reference data are plotted as lines extrapolated to high temperatures from lower-temperature measurements/simulations.

that this phase for pure oxide Li_4GeO_4 is hypothetical and metastable. According to our MLIP calculations, the *Pnma* phase is about 30 meV per atom higher in energy than the experimentally observed *Cmcm* phase.[75] To best facilitate validating our model against experimentally relevant structures that are not included in the training dataset, we specifically employ the *Cmcm* structure of Li_4GeO_4 to compute its kinetic properties. As shown in Fig. 3(e), the predictions of our model for Li-ion migration in this phase, yielding an activation energy of 0.77 ± 0.27 eV, show excellent agreement with experimental results of 0.81 eV, particularly in the higher temperature range (>900 K).[69] The calculated ionic conductivities show deviations from ideal linear Arrhenius behavior at lower temperatures. This may be attributed to an insufficient number of ion migration events occurring in that temperature range because of poor ionic conductivity properties of this material.

This successful application to materials with different space group symmetries (*e.g.*, $Pmn2_1$ and *Cmcm*) underscores the generality and versatility of the fine-tuned model. The pre-trained uMLIP provides knowledge for transfer, while fine-tuning allows for more accurate predictions and reduced errors.

Training from scratch *vs.* fine-tuning

In addition to fine-tuning, we also explored training MLIPs from scratch on the same datasets for the two benchmark material systems, NaSICON and LPGSO. Compared to fine-tuning, training from scratch generally reaches a slightly lower accuracy in both energy and force predictions (Table S2). Moreover, it is observed that models trained from scratch tend to be less stable during MD simulations, frequently resulting in unphysical behavior, *e.g.*, the divergence of the total energy. For the LPGSO system in particular, the absence of prior knowledge about Li–Li interactions leads to incorrect Li–Li pair repulsion force, which severely alters the resulting diffusion behavior and produces unphysical MD trajectories, as plotted in Fig. S6 and S7. More detailed analysis is in SI.

Exploring LIYBC system

In addition to sulfide and oxide SEs, the Li_3MX_6 family of lithium ternary halides (M = Sc, Y, In, Er, Sm–Lu; X = F, Cl, Br)[76,77] has emerged as a promising class of SSEs, owing to its distinct advantages such as high ionic conductivity, wide electrochemical stability window, and good mechanical properties.[54,78] In this section, we fine-tuned the MACE-MP model to

study the miscibility within the complex halide system comprising Li_3InCl_6, Li_3InBr_6, and Li_3YBr_6. This forms the partial ternary system $Li_3In_xY_{1-x}Br_{6y}Cl_{6-6y}$. Our investigation specifically examines compositions defined by discrete values of $x \in \{0, 0.25, 0.5, 1\}$ and $y \in \{0, 0.25, 0.5, 0.75, 1\}$, subject to the condition that $x + y \geq 1$, as illustrated in Fig. 4(b).

The three vertex compositions, namely Li_3InCl_6, Li_3InBr_6, and Li_3YBr_6, are isostructural and have all been reported to crystallize in a disordered $C2/m$ space group within a cubic close-packed (CCP) framework.[53,79] The conventional cell of each material comprises two formula units (20 atoms), with two symmetrically inequivalent Li atoms fractionally residing at positions with Wyckoff labels and multiplicities of 4g and 4h, respectively, as observed in the experimentally reported structures (ICSD: 122395 (ref. 80) for Li_3InBr_6, 29957 (ref. 80) for Li_3YBr_6).

The lowest-energy configuration for each member was identified from 2000 symmetrically distinct enumerations based on Ewald energies, encompassing configurations within the conventional cell, $1 \times 1 \times 2$, and $1 \times 2 \times 2$ supercells. The static lattice energies of those enumerations were then determined using the fine-tuned model. The validation results of the fine-tuned model are shown in Fig. S8, suggesting that a dataset of approximately 2500 samples is sufficient to train the model effectively. This is evidenced by its lower RMSE for energy, force, and stress, with error values of 0.6 meV per atom, 19.2 meV $Å^{-1}$, and 0.3 meV $Å^{-3}$, respectively.

Fig. 4(a) depicts the ball-and-stick representation of the host $C2/m$ model for the $Li_3In_xY_{1-x}Br_{6y}Cl_{6-6y}$ system. The two Li sites, 4g and 4h, are both partially occupied. The optimized lattice constants for each composition are listed in Table S4. While the equilibrium Li positions in each lowest-energy ordering may vary with composition, the arrangement of the $[MX_6]^{3-}$ building blocks remains throughout the investigated compositional range. In each stoichiometric composition, Li ions are found to preferentially occupy the interplanar 4g-type sites. Conversely, the 4h sites exhibit partial occupancy, ranging from 50% to 62.5% across different compositions. These unoccupied 4h positions thus constitute natural interstitial sites, potentially facilitating Li ion hopping. Interestingly, in the ground-state structure of $Li_3In_{0.5}Y_{0.5}Br_3Cl_3$, which features an equimolar mixture of In and Y metal cations as well as Br and Cl halides, we observed that each polyhedron is coordinated exclusively by either Br or Cl ions, with no evidence of mixed halide coordination within a single polyhedron. Instead, Cl preferentially coordinates with Y, and Br preferentially coordinates with In, forming pure $[YCl_6]^{3-}$ and $[InBr_6]^{3-}$ polyhedra, respectively (Fig. 5). This preference can perhaps be attributed to factors such as ionic size matching and specific bond strengths between the specific M–X pairs.

The phase diagram in the pseudo-ternary Li_3InCl_6–Li_3InBr_6–Li_3YBr_6 composition space is depicted in Fig. 4(b). It was found that Li_3InBr_6, Li_3YBr_6, Li_3InCl_6, $Li_3In_{0.5}Y_{0.5}Br_6$, and $Li_3In_{0.5}Y_{0.5}Br_3Cl_3$ are stable (represented by solid circles), on the convex hull relative to their constituent vertex compositions. Other compositions (in dashed circle) all exhibit only trivial E_{hull} values, not exceeding 3 meV per atom, as detailed in Table S5. Even without considering entropy at finite temperatures, the low E_{hull} values suggest these materials are metastable and synthesizable, so they are included in the further study of kinetic performance.

For the lowest-energy configurations of each composition, we performed a series of MD simulations at temperatures ranging from 800 to 1100 K, since we observed that some

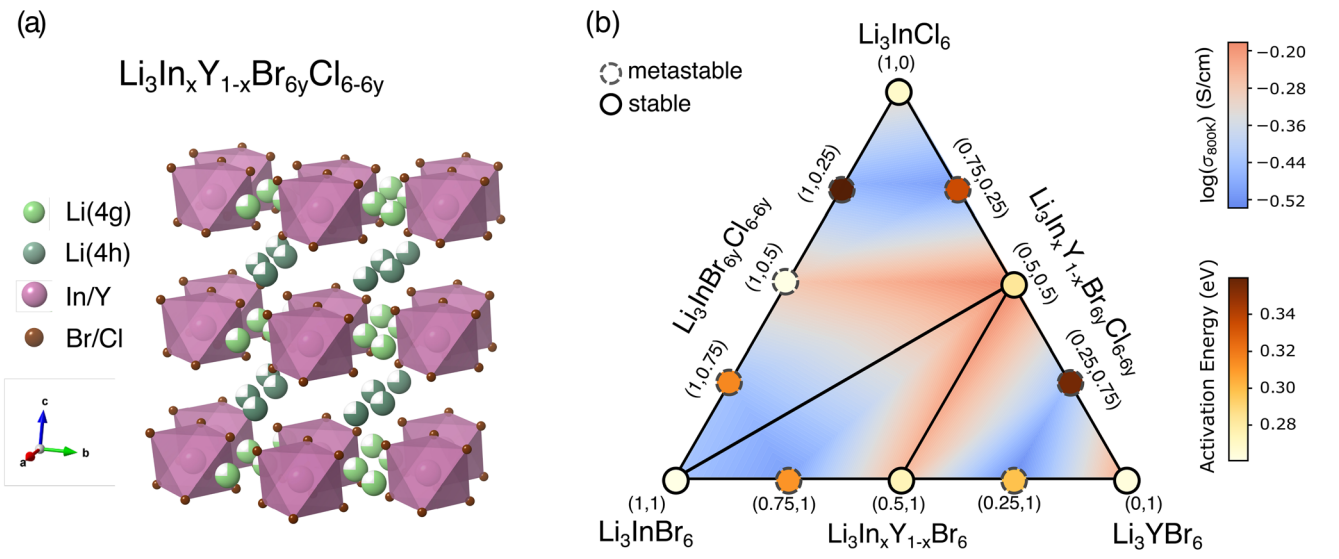

Fig. 4 (a) Crystal structure of $Li_3In_xY_{1-x}Br_{6y}Cl_{6-6y}$, with the compositional constraint $x + y \geq 1$. The two sites for Li atoms, 4g in light green and 4h in dark green, are both fractional occupied. Y/In and Br/Cl atoms are shown in pink and brown spheres, respectively. (b) Phase stability and ionic transport results of $Li_3In_xY_{1-x}Br_{6y}Cl_{6-6y}$, predicted using our fine-tuned model. Ionic conductivity data collected at 800 K is chosen as the performance metrics for this material. For each composition, a solid circle indicates a stable phase, while a dashed circle denotes a metastable phase. The color of each circle represents the activation energy for Li-ion diffusion, and the contour plot shows the predicted ionic conductivity (σ) at 800 K.

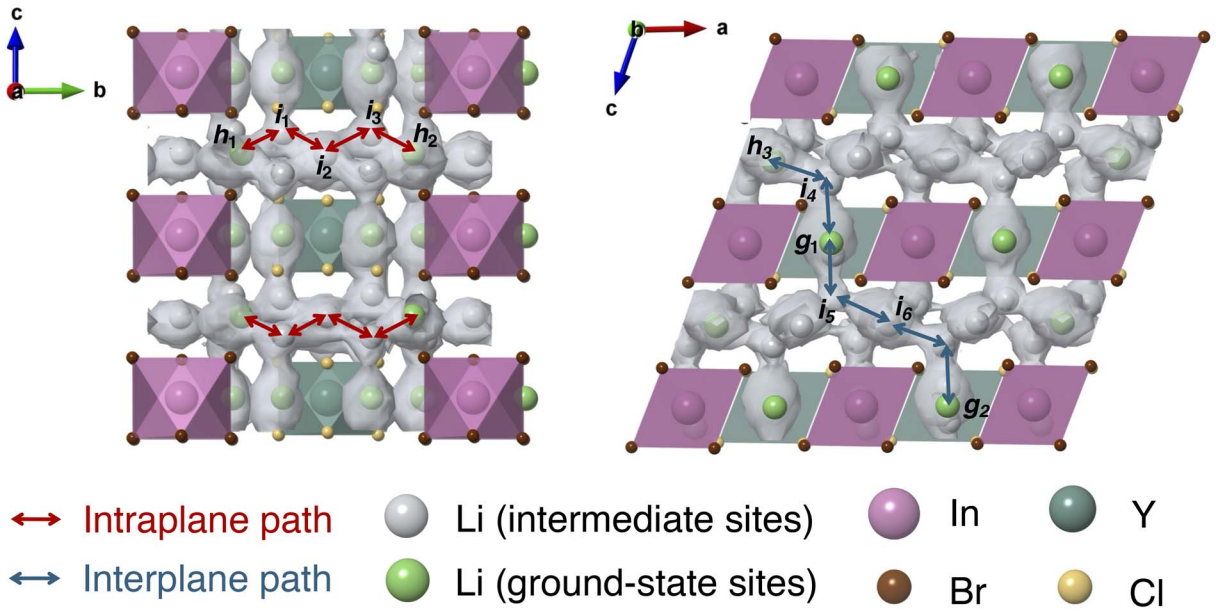

Fig. 5 The probability density of Li ions in $Li_3In_{0.5}Y_{0.5}Br_3Cl_3$, analyzed from MD trajectories at 800 K using GEMDAT. The isosurface level is set to 10^{-4} Å^{-1}. The left panel shows the view along the *a*-axis, and the right panel shows the view along the *b*-axis. Green spheres represent host Li sites in the ground-state structure, while white spheres indicate natural interstitial sites identified by GEMDAT, which are high probability Li-ion positions during the MD simulations. Two distinct migration paths are identified from this analysis: red arrows indicate intraplane pathways (4h–4h), and blue arrows indicate interplane pathways (4g–4g–4h).

compositions tend to melt at temperatures higher than 1100 K. Ionic conductivity data collected at 800 K is chosen as the performance metrics for this material. The calculated activation energy for Li ion diffusion is represented by the color in each circle in Fig. 4(b), and the contour plot, interpolated from the data on the tie-lines, shows the predicted ionic conductivity at 800 K. Arrhenius plots for each structure are presented in Fig. S9. Although ionic conductivity varies among compositions, all values remain the same order of magnitude, ranging from $\sigma = 0.3$ to 0.62 S cm^{-1} at 800 K.

The reliability of our predicted properties was validated by comparing with previously reported AIMD results for the vertex compositions, Li_3YBr_6 (ref. 81) and Li_3InCl_6.[82] As shown in Fig. S10, both the ionic conductivity and activation energy agree with AIMD results. Particularly, for Li_3YBr_6, our predicted E_a is 0.29 eV, which agrees well AIMD result of 0.28 eV. For the case of Li_3InCl_6, our predicted E_a is 0.24 eV, compared to AIMD results of 0.20 eV. Furthermore, the differences in ionic conductivity for both Li_3YBr_6 and Li_3InCl_6 between AIMD and our predictions are within the same order of magnitude, with notable overlap observed within certain temperature ranges.

Analysis of Li-ion diffusion in LIYBC system

Among the whole LIYBC system, the composition $Li_3In_{0.5}Y_{0.5}Br_3Cl_3$ shows the best ionic conductivity of ~0.62 S cm^{-1} at 800 K, along with an activation energy of 0.28 eV. Other two mixed compositions, $Li_3InBr_3Cl_3$ and $Li_3In_{0.5}Y_{0.5}Br_6$ also reaches the highest Li-ion conductivities 0.51 S cm^{-1} and 0.54 S cm^{-1} in each tie-line. This demonstrates the great potential of those mixed compositions in Li_3MX_6 systems for application as solid electrolytes. In addition, the vertex composition Li_3InCl_6 with conductivity of 0.57 S cm^{-1} also exhibits good performance.

Here, we investigate the diffusion mechanism of Li ions in $Li_3In_{0.5}Y_{0.5}Br_3Cl_3$ using MD simulation results at 800 K, with trajectory analysis performed by the GEMDAT package. Fig. 5 presents the three-dimensional probability density distribution of Li ions, where an isosurface value of 10^{-4} Å^{-3} was employed for visualization. The green spheres correspond to crystallographic host Li sites in the ground-state structure, which are mapped from the fully occupied 4g and 50% occupied 4h-type Li positions observed in experimental structures. The GEMDAT analysis of Li ion trajectories reveals that Li ions frequently visit interstitial sites adjacent to the host 4h-type sites, as indicated by the gray spheres in Fig. 5. These important interstitial sites, including those corresponding to unoccupied 4h positions, demonstrate crucial intermediates in the Li ion diffusion process within this material and are likely generalizable to other SSE systems.[83]

Two prevalent Li ion migration pathways are identified by analyzing the connectivity within the Li probability density isosurfaces and their respective occupation sites. The first pathway represents an intraplanar route connecting 4h sites within the *ab* plane, as indicated by the red arrows in the left panel of Fig. 5. The hopping of a Li ion from one host 4h site (labeled h_1) to another (h_2) is facilitated by three intermediate interstitial sites, i_1, i_2, and i_3, forming a characteristic zigzag trajectory. Notably, i_2 corresponds to a natural interstitial site derived from an unoccupied 4h position within the host lattice, while i_1 and i_3 are other symmetrically equivalent interstitial sites. The second representative pathway involves cross-plane

migration (connecting intraplanar to interplanar regions), as shown by the blue arrows in the right panel of Fig. 5, illustrating migration within the *ac* plane. This migration path consists of a hop from host 4h (labeled h_3) to host 4g (g_1), bridged by an interstitial site (i_4). The hopping then extends from g_1 to g_2 in the neighboring planes, assisted by additional intermediate sites i_5 and i_6, where the latter (i_6) is a natural interstitial 4h-type site within the structure. These two pathways discussed above are also consistent with the previous study on Li_3MX_6 family.[82] We also validate our results by performing AIMD simulations and the results are shown in Fig. S12 and S13. The probability density plots of Li ions are qualitatively consistent between MLIP-MD and AIMD.

We further quantify the Li ion transport properties by computing diffusivities and corresponding activation energies for the identified migration pathways. The planar transport characteristics (*ab*- and *ac*-plane), along with the overall three-dimensional results for comparison, are presented in Fig. S11 and Table S5. The diffusivity within a single plane surely does not represent the diffusivity along the entire migration pathway, while we use it here only for a straightforward comparison. For each composition, the diffusivities along different directions are generally within half an order of magnitude. The differences in corresponding activation energies are also comparable to the uncertainties in these activation energies. These results indicate that there is no clear directional preference for Li-ion diffusion in the LIYBC system.

Discussion and conclusions

In this work, we developed a comprehensive workflow for constructing MLIPs for disordered multi-component SSEs efficiently, which significantly reduces the time required for materials simulations from several months to a few days. The effectiveness of this approach is demonstrated through benchmarking on two complex materials systems, $Na_{1+x}Zr_2Si_xP_{3-x}O_{12}$ and $Li_{3+x}P_{1-x}Ge_xS_{4-4x}O_{4x}$. Performing MD simulations with a pre-trained uMLIP, rather than relying on AIMD, offers greater efficiency in building the training dataset for these systems. As compared in Fig. S14, for a system with the same number of atoms, running MLIP-MD with GPU can reach much higher efficiency, with almost the same accuracy as AIMD. Moreover, the current system sizes may not fully utilize the computational capacity of running MLIPs on GPUs. Larger systems are therefore expected to be handled with comparable efficiency. For each system, a dataset of approximately 2500 configurations was constructed. This dataset was sufficient to fine-tune the pre-trained PBE-level uMLIP (MACE-MP) to specific chemical spaces. High-fidelity SCAN data and a multi-head fine-tuning strategy were used in this process. Importantly, it is still recommended to perform convergence tests on the training dataset size. After fine-tuning with this proposed strategy, the formation energies and convex hulls can be obtained with low computational cost while retaining high accuracy. Overall, our model shows excellent agreement with previous experimental observations and DFT predictions of thermodynamic phase behavior. It also aligns well with experimental and AIMD results for Li/Na-ion kinetics, such as ionic conductivities and activation energies.

This agreement demonstrates that fine-tuning is an effective strategy for developing accurate MLIPs. Beyond substantially reducing computational costs, fine-tuning a uMLIP can also mitigate its sensitivity to the training data compared to training from scratch, thereby yielding improved stability and generalizability. Moreover, fine-tuning can help address systematic softening observed in uMLIPs.[84] Furthermore, by incorporating data computed at higher levels of theory, such as meta-GGA, this approach further enhances the fidelity of the resulting potential.

Building on the insights gained from benchmarking studies, we applied our workflow to a previously unexplored halide SSEs $Li_3In_xY_{1-x}Br_{6y}Cl_{6-6y}$ with $x + y \geq 1$. The anion sublattice enables both two-dimensional intralayer and three-dimensional cross-layer Li-ion migration pathways, offering desirable Li/Na-ion kinetics. Among the studied compositions, $Li_3In_{0.5}Y_{0.5}Br_3Cl_3$ exhibits the highest ionic conductivity, reaching 0.62 S cm^{-1} at 800 K. Other compositions within the compositional space also demonstrate favorable Li-ion kinetics, with conductivity lower by one order of magnitude compared to $Li_3In_{0.5}Y_{0.5}Br_3Cl_3$. Moreover, the polyanion mixing introduces configurational entropy, which could further enhance ion transport by reducing activation energies.[85] These results suggest that the $Li_3In_xY_{1-x}Br_{6y}Cl_{6-6y}$ system is promising, and merits further experimental exploration.

The MD trajectories reveal that the Li-ion diffusion in LIYBC involves both intralayer and interlayer Li-ion migration pathways. However, preference in pathways is different for different compositions. These variations arise from the distinct ground-state arrangements of anions/polyanions in each composition, which can influence factors such as diffusion bottlenecks and percolation of ion-conducting paths. Achieving optimal conductivity requires a holistic design strategy that integrates multiple factors.[86] Further investigation into the controlling factors for ionic conductivity within this system is of great importance for guiding future material design.

To summarize, we have demonstrated that our workflow for developing an MLIP combining structural enumeration with fine-tuning of pre-trained uMLIPs enables rapid and accurate exploration of complex compositional and configurational spaces. We expect that this approach will be broadly applicable to other SSEs, providing a powerful computational framework to accelerate the discovery and optimization of the next-generation solid state batteries. Furthermore, MLIPs offer significant avenues for future exploration, including the incorporation of error quantification, model distillation to enhance accuracy, and further acceleration of simulations.

Methodology

DFT calculations were performed using the Vienna *ab initio* Simulation Package (VASP), version 6.3.2.[87,88] All structures were selected from MD trajectories using MACE-MP-0a. The exchange–correlation energy in DFT was approximated by the strongly constrained and appropriately normed (SCAN) semi-

local meta-generalized gradient approximation (meta-GGA) functional.[61] Wave functions were expanded in terms of plane-wave basis set, truncated at a kinetic energy cutoff of 520 eV. Projector Augmented Wave (PAW) potentials were employed to describe core–valence electron interactions.[89] The PAW (PBE_54) potentials used were Na (19 Sep 2006, $2p^6 3s^1$), Zr (04 Jan 2005, $4s^2 4p^6 4d^2 5s^2$), Si (05 Jan 2001, $3s^2 3p^2$), P (06 Sep 2000, $3s^2 3p^3$), Li (10 Sep 2004, $1s^2 2s^1$), Ge (03 Jul 2007, $3d^{10} 4s^2 4p^2$), S (06 Sep 2000, $3s^2 3p^4$), Y (25 May 2007, $4s^2 4p^6 5s^2 4d^1$), In (06 Sep 2000, $4d^{10} 5s^2 5p^1$), Cl (06 Sep 2000, $3s^2 3p^5$), Br (06 Sep 2000, $4s^2 4p^5$), and O (08 Apr 2002, $2s^2 2p^4$). The first Brillouin zone was integrated using a Γ-centered Monkhorst–Pack homogeneous sampling with spacing of $\sim$0.2 Å^{-1} in each lattice direction. Total energies were converged within 10^{-5} eV per cell during the electronic minimization, without preserving any symmetry.

The pre-trained model used in this work is the medium-size MACE-MP-0a, trained on the MPTraj dataset.[14] To focus on the effectiveness of our fine-tuning strategy, we restrict our discussion to MACE-MP-0a, although comparisons with other pre-trained uMLIPs were also conducted.

We performed multi-head fine-tuning on this model, rather than naive fine-tuning, to avoid catastrophic forgetting.[29] The model was trained for a maximum of 500 epochs, employing an early stopping strategy if the validation loss did not improve for 20 consecutive epochs. The learning rate was set to 0.01.

For comparison, we also trained models from scratch, using an architecture closely aligned with MACE-MP-0a (medium version). Specifically, we adopted a message passing framework with 128 hidden channels, 2 interaction layers, a maximum correlation order of 3, and a radial cutoff of 5.0 Å. The training setup for models trained from scratch utilized the same learning rate and early stopping settings as the fine-tuned models.

To evaluate ionic conductivity properties, we used $2 \times 2 \times 2$ supercell models for all systems under investigation. MD simulations were performed in the canonical (*NVT*) ensemble, using a Berendsen thermostat[90] to control the temperature. For temperatures above 800 K, each simulation was run for 500 ps, which was deemed sufficient to collect statistics on ion hopping. To ensure that the system reached equilibrium, the initial 100 ps of the trajectory was discarded, and the remaining 400 ps was used for the diffusion analysis. For temperatures below 800 K, longer simulations (1 ns) were conducted to ensure adequate sampling. At these lower temperatures, the first 200 ps were excluded from further analysis.

The temperature-dependent mean squared displacement (MSD) of mobile ions of interest was calculated from their trajectories using the pymatgen package[91] based on the equation:

$$\mathrm{MSD}(T,t) = \frac{1}{N}\sum_{i=1}^{N} |\mathbf{R}_i(t) - \mathbf{R}_i(0)|^2 \quad (1)$$

where N is the number of mobile ions within the simulation cell, and $\mathbf{R}_i(t)$ is the position vector of the i-th ion at time t. The tracer diffusion coefficient, $D(T)$, is then extracted from the linear slope of the MSD as a function of time, according to the Einstein relation:

$$D(T) = \frac{1}{2n}\lim_{t\to\infty}\frac{\mathrm{d}}{\mathrm{d}t}\mathrm{MSD}(T,t) \quad (2)$$

where n represents the dimensionality of the diffusion path ($n = 3$ for three-dimensional trajectories). Specifically, for the estimation of planar diffusion (Fig. S11), we use $n = 2$ and project the trajectories onto the corresponding plane. The temperature dependence of the diffusivity was then fitted to an Arrhenius relationship to determine the activation energy, E_a, for ionic migration:

$$D(T) = D_0\, \mathrm{e}^{-E_a/(k_B T)} \quad (3)$$

where D_0 is the pre-exponential factor and k_B is the Boltzmann constant. The error bars of E_a in the figures were estimated from the standard deviation of this fitting. Furthermore, the ionic conductivity, $\sigma(T)$, is related to the diffusion coefficient by the Nernst–Einstein equation:

$$\sigma(T) = \frac{Nq^2}{Vk_B T H_r} D(T) \quad (4)$$

Here, V is the volume of the simulation cell, N is the number of mobile ions, q is the charge of the mobile ion, and H_r is the Haven ratio. The Haven ratio accounts for correlations between ionic motions, which are neglected in our analysis by assuming $H_r = 1$.

Author contributions

Z. D. designed and supervised the project. Y. D., and Z. D. performed the all the simulations with discussions with B. Z., G. S. G., and Y. L. Y. D. and Z. D. wrote the first draft. All the authors contributed to the data analysis, discussion, and final version of this manuscript.

Conflicts of interest

The authors declare no competing financial interest.

Data availability

Data for this article, including structure models used for MD simulations, interstitial sites for LIYBC analyzed from MD simulations, training datasets, and training scripts for each system, can be found at **https://doi.org/10.5281/zenodo.15771782**.

Supplementary information is available: Detailed conductivity and activation energy data, Arrhenius plots, probability density of ions for each material system; comparison between fine-tuning and training from scratch; lattice parmeters and energy above hull, 2D diffusion data of LIYBC; computation cost. See DOI: **https://doi.org/10.1039/d5ta05321h**.

Acknowledgements

Z. D. acknowledges the support from his Lee Kuan Yew Post-doctoral Fellowship (22-5930-A0001), A*STAR under its MTC-YIRG (M24N8c0108), NRF-Singapore under its Competitive

Research Programme (NRF-CRP30-2023-0001), and the Ministry of Education, Singapore, under the Academic Research Fund Tier 1 (FY2025). B. Z. acknowledges the support by the National Natural Science Foundation of China (Grant No. 12404068). Computational work involved in this research work is partially supported by NUS IT's Research Computing group using grant number NUSREC-HPC-00001.

Notes and references

1 L. C. Erhard, J. Rohrer, K. Albe and V. L. Deringer, *Nat. Commun.*, 2024, **15**, 1927.
2 Y. Zhou, W. Zhang, E. Ma and V. L. Deringer, *Nat. Electron.*, 2023, **6**, 746–754.
3 C. Chang, V. L. Deringer, K. S. Katti, V. Van Speybroeck and C. M. Wolverton, *Nat. Rev. Mater.*, 2023, **8**, 309–313.
4 V. L. Deringer, M. A. Caro and G. Csányi, *Adv. Mater.*, 2019, **31**, 1902765.
5 J. Riebesell, R. E. A. Goodall, P. Benner, Y. Chiang, B. Deng, G. Ceder, M. Asta, A. A. Lee, A. Jain and K. A. Persson, *Nat. Mach. Intell.*, 2025, **7**, 836–847.
6 J. Kim, J. Kim, J. Kim, J. Lee, Y. Park, Y. Kang and S. Han, *J. Am. Chem. Soc.*, 2025, **147**, 1042–1054.
7 A. P. Bartók, M. C. Payne, R. Kondor and G. Csányi, *Phys. Rev. Lett.*, 2010, **104**, 136403.
8 A. V. Shapeev, *Multiscale Model. Simul.*, 2016, **14**, 1153–1173.
9 H. Wang, L. Zhang, J. Han and W. E, *Comput. Phys. Commun.*, 2018, **228**, 178–184.
10 J. Behler and M. Parrinello, *Phys. Rev. Lett.*, 2007, **98**, 146401.
11 J. Gilmer, S. S. Schoenholz, P. F. Riley, O. Vinyals and G. E. Dahl, *Proceedings of the 34th International Conference on Machine Learning – Volume 70*, Sydney, NSW, Australia, 2017, pp. 1263–1272.
12 T. Xie and J. C. Grossman, *Phys. Rev. Lett.*, 2018, **120**, 145301.
13 C. Chen and S. P. Ong, *Nat. Comput. Sci.*, 2022, **2**, 718–728.
14 B. Deng, P. Zhong, K. Jun, J. Riebesell, K. Han, C. J. Bartel and G. Ceder, *Nat. Mach. Intell.*, 2023, **5**, 1031–1041.
15 S. Batzner, A. Musaelian, L. Sun, M. Geiger, J. P. Mailoa, M. Kornbluth, N. Molinari, T. E. Smidt and B. Kozinsky, *Nat. Commun.*, 2022, **13**, 2453.
16 I. Batatia, D. P. Kovacs, G. Simm, C. Ortner and G. Csanyi, *Advances in Neural Information Processing Systems*, 2022, pp. 11423–11436.
17 Y. Park, J. Kim, S. Hwang and S. Han, *J. Chem. Theory Comput.*, 2024, **20**, 4857–4868.
18 F. Fuchs, D. Worrall, V. Fischer and M. Welling, *Advances in Neural Information Processing Systems*, 2020, pp. 1970–1981.
19 R. Drautz, *Phys. Rev. B*, 2019, **99**, 014104.
20 A. Jain, S. P. Ong, G. Hautier, W. Chen, W. D. Richards, S. Dacek, S. Cholia, D. Gunter, D. Skinner, G. Ceder and K. A. Persson, *APL Mater.*, 2013, **1**, 011002.
21 S. Curtarolo, W. Setyawan, G. L. W. Hart, M. Jahnatek, R. V. Chepulskii, R. H. Taylor, S. Wang, J. Xue, K. Yang, O. Levy, M. J. Mehl, H. T. Stokes, D. O. Demchenko and D. Morgan, *Comput. Mater. Sci.*, 2012, **58**, 218–226.
22 J. E. Saal, S. Kirklin, M. Aykol, B. Meredig and C. Wolverton, *JOM*, 2013, **65**, 1501–1509.
23 J. Schmidt, H.-C. Wang, T. F. T. Cerqueira, S. Botti and M. A. L. Marques, *Sci. Data*, 2022, **9**, 64.
24 L. Barroso-Luque, M. Shuaibi, X. Fu, B. M. Wood, M. Dzamba, M. Gao, A. Rizvi, C. L. Zitnick and Z. W. Ulissi, Open Materials 2024 (OMat24) Inorganic Materials Dataset and Models, *arXiv*, 2024, preprint, arXiv:2410.12771 [cond-mat.mtrl-sci], DOI: **10.48550/arXiv.2410.12771**, **http://arxiv.org/abs/2410.12771**.
25 A. D. Kaplan, R. Liu, J. Qi, T. W. Ko, B. Deng, J. Riebesell, G. Ceder, K. A. Persson and S. P. Ong, A Foundational Potential Energy Surface Dataset for Materials, *arXiv*, 2025, preprint, arXiv:2503.04070 [cond-mat.mtrl-sci], DOI: **10.48550/arXiv.2503.04070**, **http://arxiv.org/abs/2503.04070**.
26 Z. El-Machachi, D. Frantzov, A. Nijamudheen, T. Zarrouk, M. A. Caro and V. L. Deringer, *Angew. Chem., Int. Ed.*, 2024, **63**, e202410088.
27 C. Ben Mahmoud, J. L. A. Gardner and V. L. Deringer, *Nat. Comput. Sci.*, 2024, **4**, 384–387.
28 H. Yu, M. Giantomassi, G. Matteo, J. Wang and G. Rignanese, *Mater. Genome Eng. Adv.*, 2024, **2**(3), 58.
29 I. Batatia, P. Benner, Y. Chiang, A. M. Elena, D. P. Kovács, J. Riebesell, X. R. Advincula, M. Asta, M. Avaylon, W. J. Baldwin, F. Berger, N. Bernstein, A. Bhowmik, S. M. Blau, V. Cărare, J. P. Darby, S. De, F. Della Pia, V. L. Deringer, R. Elijošius, Z. El-Machachi, F. Falcioni, E. Fako, A. C. Ferrari, A. Genreith-Schriever, J. George, R. E. A. Goodall, C. P. Grey, P. Grigorev, S. Han, W. Handley, H. H. Heenen, K. Hermansson, C. Holm, J. Jaafar, S. Hofmann, K. S. Jakob, H. Jung, V. Kapil, A. D. Kaplan, N. Karimitari, J. R. Kermode, N. Kroupa, J. Kullgren, M. C. Kuner, D. Kuryla, G. Liepuoniute, J. T. Margraf, I.-B. Magdău, A. Michaelides, J. H. Moore, A. A. Naik, S. P. Niblett, S. W. Norwood, N. O'Neill, C. Ortner, K. A. Persson, K. Reuter, A. S. Rosen, L. L. Schaaf, C. Schran, B. X. Shi, E. Sivonxay, T. K. Stenczel, V. Svahn, C. Sutton, T. D. Swinburne, J. Tilly, C. van der Oord, E. Varga-Umbrich, T. Vegge, M. Vondrák, Y. Wang, W. C. Witt, F. Zills and G. Csányi, A foundation model for atomistic materials chemistry, *arXiv*, 2024, preprint, arXiv:2401.00096 [physics.chem-ph], DOI: **10.48550/arXiv.2401.00096**, **http://arxiv.org/abs/2401.00096**.
30 X. Fu, B. M. Wood, L. Barroso-Luque, D. S. Levine, M. Gao, M. Dzamba and C. L. Zitnick, Learning Smooth and Expressive Interatomic Potentials for Physical Property Prediction, *arXiv*, 2025, preprint, arXiv:2502.12147 [physics.comp-ph], DOI: **10.48550/arXiv.2502.12147**, **http://arxiv.org/abs/2502.12147**.
31 S. Gong, Y. Zhang, Z. Mu, Z. Pu, H. Wang, X. Han, Z. Yu, M. Chen, T. Zheng, Z. Wang, L. Chen, Z. Yang, X. Wu, S. Shi, W. Gao, W. Yan and L. Xiang, *Nat. Mach. Intell.*, 2025, **7**, 543–552.
32 T. Famprikis, P. Canepa, J. A. Dawson, M. S. Islam and C. Masquelier, *Nat. Mater.*, 2019, **18**, 1278–1291.
33 J. C. Bachman, S. Muy, A. Grimaud, H.-H. Chang, N. Pour, S. F. Lux, O. Paschos, F. Maglia, S. Lupart, P. Lamp, L. Giordano and Y. Shao-Horn, *Chem. Rev.*, 2016, **116**, 140–162.

34 Q. Zhao, S. Stalin, C.-Z. Zhao and L. A. Archer, *Nat. Rev. Mater.*, 2020, **5**, 229–252.
35 Y. He, Q. Chen and W. Lai, *Solid State Ionics*, 2023, **399**, 116298.
36 L. Xu, W. Shao, H. Jin and Q. Wang, *J. Phys. Chem. C*, 2023, **127**, 24106–24117.
37 A. P. Maltsev, I. V. Chepkasov and A. R. Oganov, *ACS Appl. Mater. Interfaces*, 2023, **15**, 42511–42519.
38 J. Choi, B. Jun and Y. Jung, *Chem. Eng. J.*, 2025, **516**, 163847.
39 Z. A. H. Goodwin, M. B. Wenny, J. H. Yang, A. Cepellotti, J. Ding, K. Bystrom, B. R. Duschatko, A. Johansson, L. Sun, S. Batzner, A. Musaelian, J. A. Mason, B. Kozinsky and N. Molinari, *J. Phys. Chem. Lett.*, 2024, **15**, 7539–7547.
40 J. Wang, A. A. Panchal, G. S. Gautam and P. Canepa, *J. Mater. Chem. A*, 2022, **10**, 19732–19742.
41 A. Seth, R. P. Kulkarni and G. S. Gautam, *ACS Mater. Au*, 2025, **5**, 458–468.
42 A. C. C. Dutra, B. A. Goldmann, M. S. Islam and J. A. Dawson, *Nat. Rev. Mater.*, 2025, 1–18.
43 J. B. Goodenough, H. Y.-P. Hong and J. A. Kafalas, *Mater. Res. Bull.*, 1976, **11**, 203–220.
44 Z. Deng, T. P. Mishra, E. Mahayoni, Q. Ma, A. J. K. Tieu, O. Guillon, J.-N. Chotard, V. Seznec, A. K. Cheetham, C. Masquelier, G. S. Gautam and P. Canepa, *Nat. Commun.*, 2022, **13**, 4470.
45 Z. Wang, S. Park, Z. Deng, D. Carlier, J.-N. Chotard, L. Croguennec, G. S. Gautam, A. K. Cheetham, C. Masquelier and P. Canepa, *J. Mater. Chem. A*, 2022, **10**, 209–217.
46 Z. Wang, T. P. Mishra, W. Xie, Z. Deng, G. S. Gautam, A. K. Cheetham and P. Canepa, *ACS Mater. Lett.*, 2023, **5**, 2499–2507.
47 B. Ouyang, J. Wang, T. He, C. J. Bartel, H. Huo, Y. Wang, V. Lacivita, H. Kim and G. Ceder, *Nat. Commun.*, 2021, **12**, 5752.
48 Q. Ma, C.-L. Tsai, X.-K. Wei, M. Heggen, F. Tietz and J. T. S. Irvine, *J. Mater. Chem. A*, 2019, 7766–7776.
49 J. P. Boilot, G. Collin and P. Colomban, *J. Solid State Chem.*, 1988, **73**, 160–171.
50 Y. Li, Z. Deng and C. Chen, *Chem. Mater.*, 2024, **36**, 7877–7886.
51 Y. Tomita, A. Fuji-i, H. Ohki, K. Yamada and T. Okuda, *Chem. Lett.*, 1998, **27**, 223–224.
52 K. Yamada, K. Kumano and T. Okuda, *Solid State Ionics*, 2006, **177**, 1691–1695.
53 Y. Tomita, H. Matsushita, K. Kobayashi, Y. Maeda and K. Yamada, *Solid State Ionics*, 2008, **179**, 867–870.
54 X. Li, J. Liang, X. Yang, K. R. Adair, C. Wang, F. Zhao and X. Sun, *Energy Environ. Sci.*, 2020, **13**, 1429–1461.
55 J. O. Bonsu, A. Bhadra and D. Kundu, *Adv. Sci.*, 2024, **11**, 2403208.
56 R. E. Skyner, J. B. O. Mitchell and C. R. Groom, *CrystEngComm*, 2017, **19**, 641–652.
57 P. Molaiyan, S. E. Mailhiot, K. Voges, A. M. Kantola, T. Hu, P. Michalowski, A. Kwade, V.-V. Telkki and U. Lassi, *Mater. Des.*, 2023, **227**, 111690.
58 X. Li, J. Liang, J. Luo, M. N. Banis, C. Wang, W. Li, S. Deng, C. Yu, F. Zhao, Y. Hu, T.-K. Sham, L. Zhang, S. Zhao, S. Lu, H. Huang, R. Li, K. R. Adair and X. Sun, *Energy Environ. Sci.*, 2019, **12**, 2665–2671.
59 F. Stainer and H. M. R. Wilkening, *Phys. Rev. B*, 2024, **109**, 174304.
60 F. Musil, A. Grisafi, A. P. Bartók, C. Ortner, G. Csányi and M. Ceriotti, *Chem. Rev.*, 2021, **121**, 9759–9815.
61 J. Sun, A. Ruzsinszky and J. Perdew, *Phys. Rev. Lett.*, 2015, **115**, 036402.
62 J. P. Perdew, K. Burke and M. Ernzerhof, *Phys. Rev. Lett.*, 1996, **77**, 3865–3868.
63 X. Huang, B. Deng, P. Zhong, A. D. Kaplan, K. A. Persson and G. Ceder, Cross-functional transferability in universal machine learning interatomic potentials, *arXiv*, 2025, preprint, arXiv:2504.05565 [cond-mat.mtrl-sci], DOI: **10.48550/arXiv.2504.05565**, **http://arxiv.org/abs/2504.05565**.
64 V. Azizi, S. Smeets, A. K. Lavrinenko, S. Ciarella, T. Famprikis, V. Landgraf and A. Vasileiadis, *GEMDAT*, 2025, **https://zenodo.org/records/15235004**.
65 L. Pradhan and P. Padma Kumar, *J. Phys. Chem. C*, 2025, **129**, 13756–13767.
66 J.-S. Kim, W. D. Jung, S. Choi, J.-W. Son, B.-K. Kim, J.-H. Lee and H. Kim, *J. Phys. Chem. Lett.*, 2018, **9**, 5592–5597.
67 N. J. de Klerk, E. van der Maas and M. Wagemaker, *ACS Appl. Energy Mater.*, 2018, **1**, 3230–3242.
68 B. Zhang, M. Weng, Z. Lin, Y. Feng, L. Yang, L.-W. Wang and F. Pan, *Small*, 2020, **16**, 1906374.
69 S. B. Yahya, I. Garoui, M. Zaghrioui, A. Oueslati and B. Louati, *RSC Adv.*, 2025, **15**, 9295–9304.
70 Y. Liu, X. He and Y. Mo, *npj Comput. Mater.*, 2023, **9**, 1–13.
71 K. Homma, M. Yonemura, T. Kobayashi, M. Nagao, M. Hirayama and R. Kanno, *Solid State Ionics*, 2011, **182**, 53–58.
72 T. Kimura, T. Inaoka, R. Izawa, T. Nakano, C. Hotehama, A. Sakuda, M. Tatsumisago and A. Hayashi, *J. Am. Chem. Soc.*, 2023, **145**, 14466–14474.
73 N. D. Lepley, N. A. W. Holzwarth and Y. A. Du, *Phys. Rev. B: Condens. Matter Mater. Phys.*, 2013, **88**, 104103.
74 J. H. Kim, B. Jun, Y. J. Jang, S. H. Choi, S. H. Choi, S. M. Cho, Y.-G. Kim, B.-H. Kim and S. U. Lee, *Nano Energy*, 2024, **124**, 109436.
75 I. M. Hodge, M. D. Ingram and A. R. West, *J. Am. Ceram. Soc.*, 1976, **59**, 360–366.
76 T. Asano, A. Sakai, S. Ouchi, M. Sakaida, A. Miyazaki and S. Hasegawa, *Adv. Mater.*, 2018, **30**, 1803075.
77 X. He, Y. Zhu and Y. Mo, *Nat. Commun.*, 2017, **8**, 15893.
78 R. Li, P. Lu, X. Liang, L. Liu, M. Avdeev, Z. Deng, S. Li, K. Xu, J. Feng, R. Si, F. Wu, Z. Zhang and Y.-S. Hu, *ACS Energy Lett.*, 2024, **9**, 1043–1052.
79 T. Jeon and S. C. Jung, *J. Mater. Chem. A*, 2023, **11**, 4334–4344.
80 B. Helm, R. Schlem, B. Wankmiller, A. Banik, A. Gautam, J. Ruhl, C. Li, M. R. Hansen and W. G. Zeier, *Chem. Mater.*, 2021, **33**, 4773–4782.
81 S. Wang, Q. Bai, A. M. Nolan, Y. Liu, S. Gong, Q. Sun and Y. Mo, *Angew. Chem., Int. Ed.*, 2019, **58**, 8039–8043.

82 D. Park, H. Park, Y. Lee, S.-O. Kim, H.-G. Jung, K. Y. Chung, J. H. Shim and S. Yu, *ACS Appl. Mater. Interfaces*, 2020, **12**, 34806–34814.
83 Y. Li and N. A. W. Holzwarth, *Phys. Rev. Mater.*, 2022, **6**, 025401.
84 B. Deng, Y. Choi, P. Zhong, J. Riebesell, S. Anand, Z. Li, K. Jun, K. A. Persson and G. Ceder, *npj Comput. Mater.*, 2025, **11**, 9.
85 Y. Zeng, B. Ouyang, J. Liu, Y.-W. Byeon, Z. Cai, L. J. Miara, Y. Wang and G. Ceder, *Science*, 2022, **378**, 1320–1324.
86 K. Jun, Y. Chen, G. Wei, X. Yang and G. Ceder, *Nat. Rev. Mater.*, 2024, 1–19.
87 G. Kresse and J. Furthmüller, *Comput. Mater. Sci.*, 1996, **6**, 15–50.
88 G. Kresse and J. Furthmüller, *Phys. Rev. B: Condens. Matter Mater. Phys.*, 1996, **54**, 11169–11186.
89 G. Kresse and D. Joubert, *Phys. Rev. B: Condens. Matter Mater. Phys.*, 1999, **59**, 1758–1775.
90 H. J. C. Berendsen, J. P. M. Postma, W. F. Van Gunsteren, A. DiNola and J. R. Haak, *J. Chem. Phys.*, 1984, **81**, 3684–3690.
91 S. P. Ong, W. D. Richards, A. Jain, G. Hautier, M. Kocher, S. Cholia, D. Gunter, V. L. Chevrier, K. A. Persson and G. Ceder, *Comput. Mater. Sci.*, 2013, **68**, 314–319.

